Rahman, B. M., Kejalakshmy, N., Uthman, M., Agrawal, A., Wongcharoen, T. & Grattan, K. T. (2009). Mode degeneration in bent photonic crystal fiber study by using the finite element method. Applied Optics, 48(31), G131 - G138. doi: 10.1364/AO.48.00G131 <http://dx.doi.org/10.1364/AO.48.00G131>

Mode degeneration in bent photonic crystal fiber study by using the finite element method

B. M. Azizur Rahman,[1,*] Namassivayane Kejalakshmy,[1] Muhammad Uthman,[1] Arti Agrawal,[1] Tiparatana Wongcharoen,[2] and Kenneth T. V. Grattan[1]

[1]School of Engineering and Mathematical Sciences, City University London, Northampton Square, London EC1V 0HB, UK

[2]Department of Electrical Engineering, Bangkok University, Bangkok, Thailand

*Corresponding author: B.M.A.Rahman@city.ac.uk

Received 16 June 2009; revised 16 September 2009; accepted 12 October 2009; posted 14 October 2009 (Doc. ID 112866); published 23 October 2009

The development of highly dispersive lower and higher order cladding modes and their degeneration with respect to the fundamental core mode in a bent photonic crystal fiber is rigorously studied by use of the full-vectorial finite element method. It is shown that changes in the bending radius can modify the modal properties of large-area photonic crystal fibers, important for a number of potential practical applications. © 2009 Optical Society of America

OCIS codes: 060.5295, 060.0060.

1. Introduction

Photonic crystal fibers (PCFs) [1] are seen as potentially important specialized optical waveguides due to their inherent advantages arising from their modal properties, such as controllable spot size, birefringence, and their dispersion properties, achieved through tailoring their structural parameters. In many practical applications, such PCFs will encounter bends, twists, and stress. It is also well known that when a fiber is bent, the modal field shifts in the outward direction and suffers from radiation loss. One of the main disadvantages suffered by standard silica fiber has been that significant bending loss arises due to the low index contrast between the core and the cladding when compared to that of a PCF. However, sometimes the need for a small bending radius may be unavoidable in a specific optical waveguide: on the other hand, bending effects have also been exploited to design functional devices such as ring resonators [2], arrayed waveguide filters [3], optical delay lines [4], S-bend attenuators [5], or to suppress higher order modes [6]. Similarly, efforts have also been expended to better understand the behavior of bent PCFs [7–9]. We report on the variation of the key modal parameters in such fibers that arises from the change in the coupling between the fundamental core mode and the localized cladding mode across the airholes: this analysis is done by using a rigorous full-vectorial finite element method.

Numerical Solutions. Various methods have been considered to date in the study of the modal characteristics of PCFs. One of the first methods used was the effective index method [10], which is a scalar field approach that treats the PCF as an equivalent step-index fiber but that cannot yield the actual modal field profile and the modal birefringence of the PCF. The plane wave method (PWM) [11], a more widely used approach, requires a larger "supercell" that demands the periodicity of the PCF cladding and suffers from an inefficient computation time. The localized basis function method [12], the multipole method [13], and the supercell lattice method [14] are more effective methods than the PWM, but these methods have limitations in defining practical PCFs with a finite lattice period. These methods are often unable to consider an arbitrary transverse variation of the PCF cross section, such

0003-6935/09/31G131-08$15.00/0

as is required in describing noncircular airholes or nonidentical multiple defects. On the other hand, the more powerful and versatile finite difference method (FDM) [15], the finite element method (FEM) [16], and the beam propagation method (BPM) [17] are more effective when studying such complex microstructured fibers. A full-vectorial FEM [18] can be used efficiently in determining the quasi-TE and quasi-TM fundamental and higher order modes. A real value eigenvalue problem determined by the H field formulation can be solved with higher computing efficiency, compared to other methods, in determining important modal properties of a PCF such as the effective index, spot size, dispersion, and cutoff of fundamental and higher order modes [19].

In the modal solution approach based on the FEM, the intricate cross section of a PCF can be accurately represented by using nearly a million triangles of different shapes and sizes. The flexibility of the irregular mesh makes the FEM preferable when compared to the FDM, which not only uses inefficient regular spaced meshing, but also cannot be used to represent adequately slanted or curved dielectric interfaces of the airholes. The optical modes in a PCF with two-dimensional confinement and high index contrast air/silica interfaces are also hybrid in nature, with all six components of the E and H fields being present. Hence, only a vectorial formulation should be used to calculate accurately PCF modal solutions. The H field formulation with the augmented penalty function technique is given below [18]:

$$\omega^2 = \frac{\left(\int(\nabla \times \vec{H}) * \cdot \hat{\varepsilon}^{-1}(\nabla \times \vec{H})\mathrm{d}\Omega\right) + \left(\int(\eta/\varepsilon_o)(\nabla \cdot \vec{H}) * (\nabla \cdot \vec{H})\mathrm{d}\Omega\right)}{\int \vec{H} * \cdot \hat{\mu}\vec{H}\mathrm{d}\Omega}, \tag{1}$$

where $\vec{H}$ is the full-vectorial magnetic field, $\hat{\varepsilon}$ and $\hat{\mu}$ are the permittivity and permeability, respectively, of the waveguide, ε_0 is the permittivity of the free-space, and ω^2 is the eigenvalue, where ω is the angular frequency of the wave. The dimensionless parameter η is used to impose the divergence-free condition of the magnetic field in a least squares sense to eliminate spurious solutions. A highly efficient sparse solver with the subspace iteration technique is used to solve the resulting large eigenvalue equations with orders often larger than 100,000.

To study arbitrary bends, various numerical methods have been developed and used to simulate the light propagation in bent waveguides with the aim of characterizing the bending, transition, and polarization losses. The conformal transformation [20] has most widely been used to represent such bent waveguides by converting a curved dielectric waveguide to its equivalent straight waveguide with a modified index profile. The coordinate transformation allows a bent optical waveguide in the x plane to be represented by an equivalent straight waveguide with modified refractive index distribution, $n_{\mathrm{eq}}(x,y)$:

$$n_{\mathrm{eq}}(x,y) = n(x,y)\left(1 + \frac{x}{R}\right), \tag{2}$$

where $n(x,y)$ is the original refractive index profile of the bent waveguide, $n_{\mathrm{eq}}(x,y)$ is the equivalent index profile of a straight guide, R is the radius of the curvature, and x is the distance from the center of the waveguide. This equation is valid for the range $2x \ll R$, which is well within the ranges considered in this paper. Subsequently, the straight waveguide with a transformed index profile can be analyzed by a number of modal solution techniques, such as the eigenmode expansion [21], the methods of lines [22], the FDM [23], the variational method [24], the matrix approach [25], the Wentzel–Kramers–Brillouin (WKB) analysis [26], and the FEM approach [27–29]. The beam propagation approach [30,31] has been used successfully, but this makes the problem three dimensional (3D) with additional computational costs. Similarly the finite-difference time-domain (FDTD) [32] approach has also been used, but with the inclusion of an additional time variation, it is more computer intensive than the modal solution or the BPM approaches.

When a waveguide is bent, change in the refractive index due to the elasto-optic effect can also increase the modal loss [33]. This can be represented by modifying the bending radius value by a simple linear transformation, as reported earlier [34]:

$$\begin{aligned} n_{\mathrm{eq}}(x,y) &= n(x,y)\left[1 + (1-\chi)\left(\frac{x}{R}\right)\right] \\ &= n(x,y)\left(1 + \frac{x}{R'}\right). \end{aligned} \tag{3}$$

When the linear coefficient value χ is taken as -0.22 for silica [34], then the modified R' would be $1-\chi$ times or 1.22 times smaller than the actual bending radius, R.

In the original **H**-field formulation [18], which considered a real eigenvalue equation, the perfectly

matched layer (PML) [35,36] can be introduced around the orthodox computation window. The PML allows the electromagnetic waves to leak out of the bent waveguides and avoids the reflection at the hard boundary of the orthodox computational window by using the bi-anisotropic constitutive parameters that results in a set of perfectly matched permeability and permittivity tensors [35,36], which is also equivalent to coordinate stretching [37]. This allows the calculation of the power loss out of the computation window, but the introduction of the complex refractive index in the PML region also modifies the real eigenvalue to a complex eigenvalue equation. The modal loss value is calculated from the imaginary part (α) of the complex propagation constant $\gamma = \beta + j\alpha$. The width of the PML layer has been chosen such that the modal solutions are stable with respect to the variations of the PML and the refractive indices of the local elements in the PML layer are matched with the local refractive indices at the edge of the cladding. Only one-half of the PCF cross section is considered here, as the existing onefold mirror symmetry of a bent PCF has been exploited.

2. Results

In this study, silica photonic crystal fiber with airholes arranged in a triangular lattice is considered, with the diameter of airhole denoted by d and distance between two airholes given by Λ. The refractive index of silica is taken as 1.444 at the operating wavelength of 1.55 μm. It has been reported earlier [28] that, when d/Λ is lower than 0.42, a PCF can only support two fundamental $H^y{}_{11}$ (quasi-TE) and $H^x{}_{11}$ (quasi-TM) modes for all the values of pitch length Λ; however, for higher Λ and d/Λ values, it can also support additional higher order modes of a given polarization.

It is well known that such a PCF suffers from leakage loss as the modal index is lower than the refractive index of the outer cladding silica region. This leakage loss can be reduced by increasing the number of airhole rings or considering a well confined mode operating far away from its cutoff condition. It is also well known that an optical waveguide suffers from increased bending loss as its bending radius is reduced. The variations of the total loss for the fundamental quasi-TM ($H^x{}_{11}$) mode with the bending radius R, for three different pitch values, are shown in Fig. 1. In this case N is the number of airhole rings, and the d/Λ is taken to be constant and equal to 0.5. For a lower pitch length, $\Lambda = 1.6\,\mu$m, the bending loss increases monotonically as the bending radius is reduced. However, in this case, the leakage loss (for a straight waveguide or when R is very large) is also high as the PCF is operating close to its modal cutoff. Using a PCF with such a smaller pitch length is often not preferred due to its higher leakage losses. As the pitch length is increased, for $\Lambda = 2.6\,\mu$m, the leakage loss is reduced by 3 orders of magnitude (at $R = 10^4\,\mu$m the total loss contains mainly the leakage loss, as the pure bending loss is nearly zero).

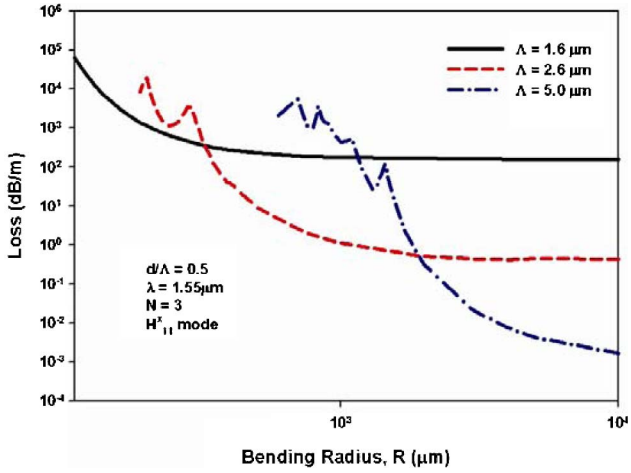

Fig. 1. (Color online) Variation of the total losses with the bending radius R for the quasi-TM modes.

For this case, as the bending radius is reduced, the bending loss increases progressively, and as a result the total loss also increases. It can be noted that increases in the bending loss with the bending radius are more rapid as the bending radius is reduced, compared to the case with a lower pitch length, $\Lambda = 1.6\,\mu$m. At a lower bending radius, the nonmonotonic nature is also seen with oscillations in the total loss values. In these cases, it has been observed that the modal and leakage properties of both the quasi-TE and the quasi-TM modes are almost similar along with the transition in their loss properties, also at similar locations. When the pitch length is increased further, for $\Lambda = 5.0\,\mu$m the leakage loss is significantly reduced to 10^{-3} dB/m, and a PCF with a larger dimension is often then preferred. However, in this case the PCF is more susceptible to bending, and the total loss value increases rapidly as the bending radius is reduced: for some fixed radii, this value can even be higher than that of a PCF with a lower pitch value. However, in this case of a larger Λ, the oscillations in the loss values are more frequent and appear to be random in nature. Similar features have also been observed experimentally [9].

To study mode degeneration more closely, the smaller bending radius range is considered in some further detail using an expanded range and creating many additional simulated results. The variation of the effective index for the quasi-TM mode with the bending radius is shown in Fig. 2. In this region, two distinct modes can be easily identified (their field profiles are shown below). The solid line in Fig. 2 represents the first $H^x{}_1$ eigenmode, with a higher effective index, and the second eigenmode, $H^x{}_2$, is shown by a dashed line: it has a lower effective index for the range of bending radius shown here. In a way similar to the formation of the even and odd-like supermodes of two nonidentical coupled waveguides [7], these two curves never cross each other, but these two modes go through a transition near $R \sim 1445\,\mu$m, when they are phase matched. The horizontal sections of these two lines represent the $H^x{}_{11}$ core mode confined at

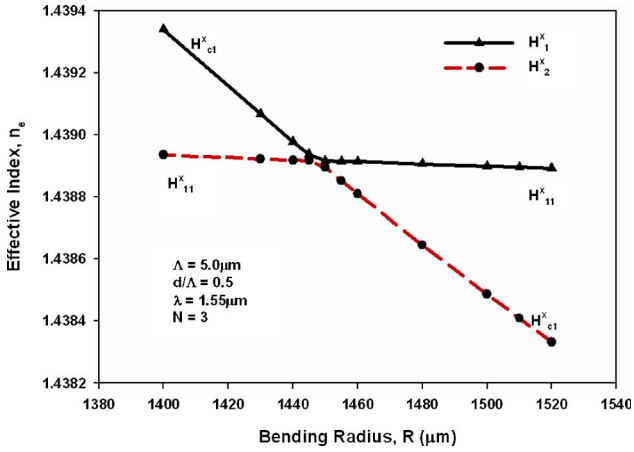

Fig. 2. (Color online) Variation of the effective indices with the bending radius R.

the center of the PCF. The slanted line represents a highly dispersive $H^x{}_{c1}$ cladding mode, which is located on the right side of the core and between the two airholes for a bent PCF. This cladding mode has a smaller core area but with a progressively higher local equivalent refractive index value as the bending radius is reduced. For a specific bending radius, the effective index of this cladding mode becomes equal to that of the core mode, and they become degenerate. It should be noted that the dispersion properties of the TE and TM polarized modes for both the core and the cladding modes are similar.

The loss values for these first $H^x{}_1$ and second $H^x{}_2$ modes are shown in Fig. 3 by a solid and a dashed line, respectively. Parts of these two curves form the lower section, which shows the loss values of the $H^x{}_{11}$ core mode, is around 100 dB/m. On the other hand, the upper lines represent the $H^x{}_{c1}$ cladding modes with significantly higher loss values, around 12000 dB/m. However, these two curves also go through a transition near $R \sim 1445\,\mu$m, which is similar to the effective index curves shown in Fig. 2. The upper curve goes through a local minimum (which is not clearly visible) near the mode degeneration point, being mixed with a less lossy $H^x{}_{11}$ core mode. Similarly the loss value of the lower curve also peaks near the resonance due to being mixed with a highly lossy cladding mode. This local peak is clearly shown in Fig. 1 for $\Lambda = 5\,\mu$m around a value of $R = 1445\,\mu$m. In a similar way for the transition in the effective indices and loss values, the spot sizes of these modes also go through a transition. There are different alternative definitions for the mode-size area, such as the spot size, σ, and the effective area, A_{eff}. Here the spot size is defined as the area with a power density greater than $1/e^2$ times its maximum value, and the effective area, A_{eff}, [38] is defined as

$$A_{\text{eff}} = \frac{\left(\iint_s |E_t|^2 \mathrm{d}x\mathrm{d}y\right)^2}{\left(\iint_s |E_t|^4 \mathrm{d}x\mathrm{d}y\right)}, \tag{4}$$

where $\mathbf{E}_t$ represents the transverse electric field vectors and S represents the whole fiber area cross section. Although for a circular and Gaussian mode shape they may yield similar values, for a noncircular, non-Gaussian, or for a nonmonotonic mode shape profile, they can yield different values. However, as a mode transforms from core mode to cladding mode or vice versa, all these parameters also show rapid changes when the modes degenerate.

The variation of the H_x field for the $H^x{}_{11}$ core mode along the center of the guide in the x direction is shown in Fig. 4 when $R = 1460\,\mu$m. It can be observed that field is predominantly confined at the center of the PCF core: however, its maximum value is shifted slightly to the right of the waveguide center, shown by an arrow. Two local peaks are also visible and are located in the silica bridge region between the first and second airhole rings and the second and third airhole rings (shown as 1, 2, and 3 in the figure), respectively. These peaks are only visible on the right of the core, not on the left side, which can be understood by considering that in

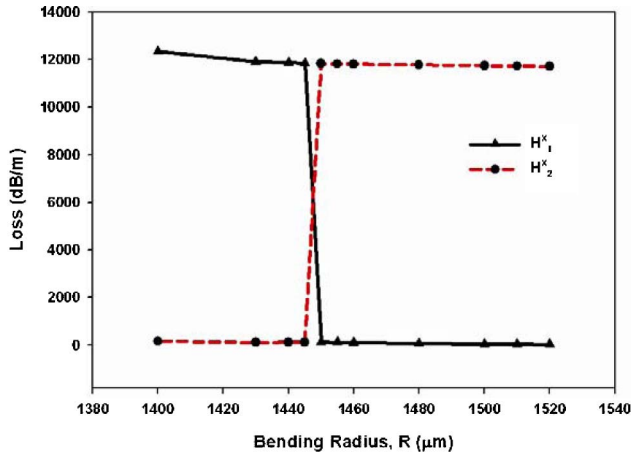

Fig. 3. (Color online) Variation of the total losses with the bending radius R.

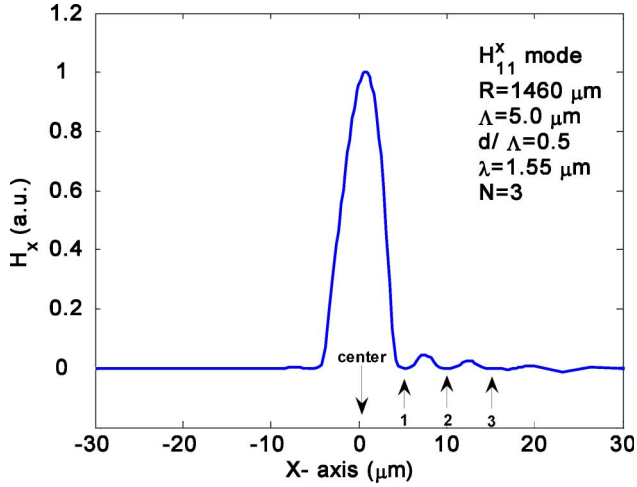

Fig. 4. (Color online) H_x field profile of the $H^x{}_{11}$ core mode along the X axis through the center of the core when $R = 1460\,\mu$m.

the conformal transformation, the higher local equivalent index value allows such local modes to be formed on the right side of the core. Its spot size and effective area are 31.5 and 30.0 μm^2, respectively.

At this particular bending radius (where $R = 1460\,\mu m$), a local cladding mode also exists with its effective index slightly lower than the $H^x{}_{11}$ core mode. The H_x field contour for this $H^x{}_{c1}$ cladding mode is shown in Fig. 5. The locations of the airholes are shown by circles. It can clearly be observed that this cladding mode is formed between the airholes of the second and third rings. The spot-size area of this mode is smaller ($\sigma = 26.1\,\mu m^2$), being restricted to a smaller silica bridging region (but its $A_{eff} = 37.4\,\mu m^2$ is rather large as the field spreads slowly), but this mode is highly dispersive with a higher loss value.

When the bending radius is reduced below the degeneration point ($R < 1445\,\mu m$) the effective index of the cladding mode becomes higher than that of the $H^x{}_{11}$ core mode, and the eigenvalues change their positions. The 3D H_x field profile of the $H^x{}_{11}$ core mode, when $R = 1430\,\mu m$, is shown in Fig. 6. The local peaks on the right of the main peak are visible. However, it can be observed that the sign of second peak in the cladding area is negative, which is also an indication of the change in mode order.

The 3D H_x field profile of the $H^x{}_{c1}$ cladding mode, when $R = 1430\,\mu m$, is shown in Fig. 7. Its narrower peak, existing between two airholes (marked by 1 and 2), is clearly visible. Besides that, one local peak in the core region and another between the second and the third airhole rings are also visible.

It has been mentioned that the modal properties of the quasi-TM and quasi-TM modes are almost identical, as the original straight PCF has a sixfold rotational symmetry, before the effect of bending is considered. In Fig. 1, it is also noted that the bending loss curve for $\Lambda = 5\,\mu m$ shows several local perturbations. To study this more thoroughly, the bending radius is further reduced, and the variations of

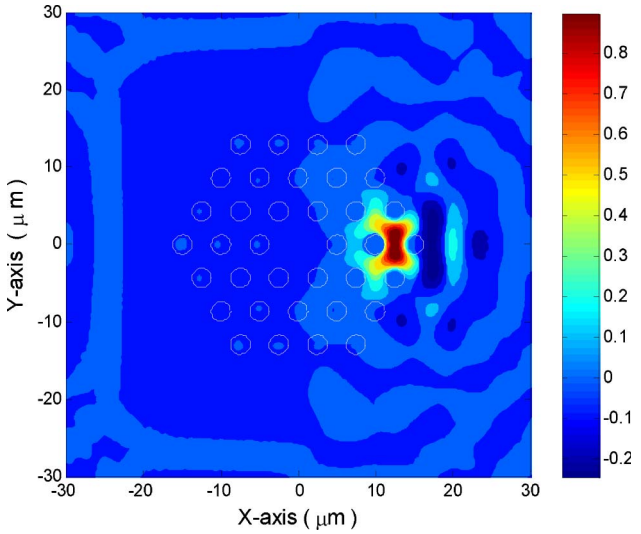

Fig. 5. (Color online) H_x field contour for $H^x{}_{c1}$ cladding mode when $R = 1460\,\mu m$.

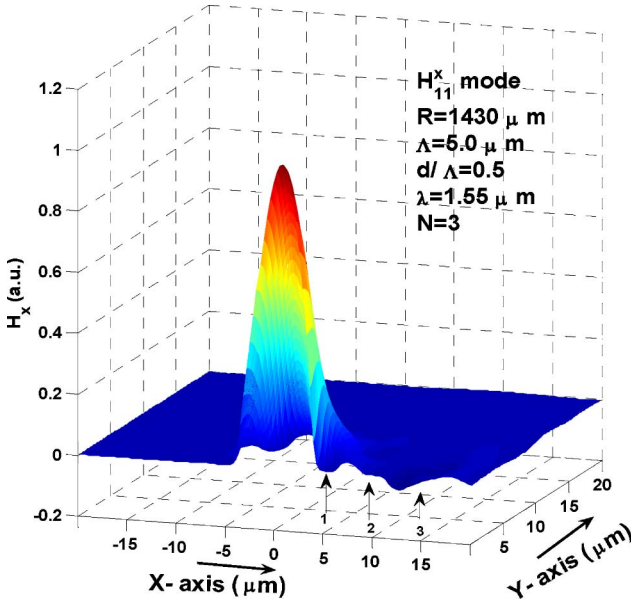

Fig. 6. (Color online) H_x field profile for the $H^x{}_{11}$ core mode when $R = 1430\,\mu m$.

the effective index values for the other polarization, quasi-TE core, and cladding modes are shown in Fig. 8. The effective index variations of the first $H^y{}_1$ and second $H^y{}_2$ modes are shown by a dashed and a solid line, respectively. It can be noted that the effective index of the fundamental core mode is higher than that shown in Fig. 2, as the bending radius is now significantly reduced. In a similar way to what is shown in Fig. 2, these two effective index curves do not cross each other but transform from the $H^y{}_{11}$ core mode to the $H^y{}_{c2}$ cladding mode or vice versa around a value of $R \sim 835\,\mu m$. The lower bending radius further increases the local refractive index on the right-side of the PCF center. The dispersion slope

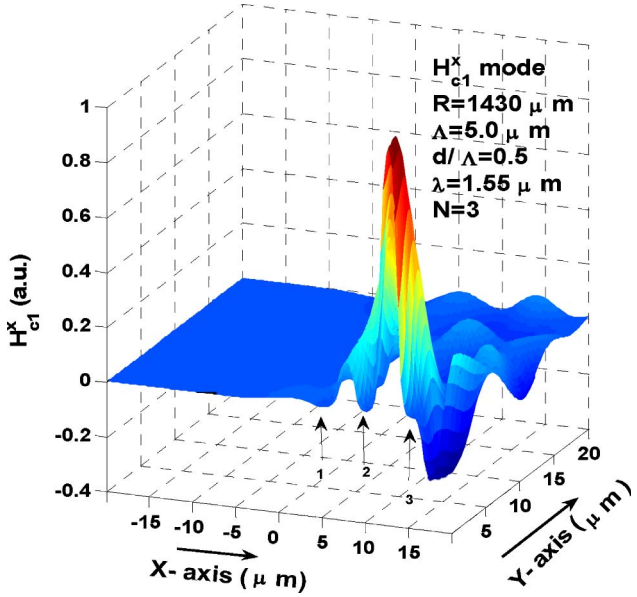

Fig. 7. (Color online) H_x field profile for the $H^x{}_{c1}$ cladding mode when $R = 1430\,\mu m$.

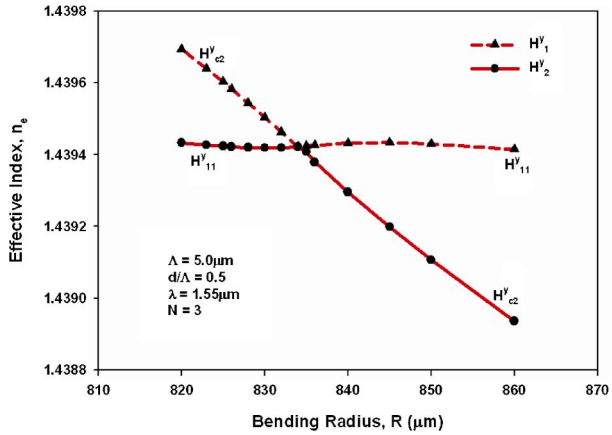

Fig. 8. (Color online) Variation of the effective indices with the bending radius for the quasi-TE modes.

of the $H^y{}_{c2}$ cladding mode is also higher in this case than that of the $H^x{}_{c1}$ cladding mode.

The variations of the total loss values for the $H^y{}_{11}$ core and $H^y{}_{c2}$ cladding modes are shown in Fig. 9. In this case, the core mode with a lower loss value transforms to a higher loss cladding mode near the degeneration position. In this case, the $H^y{}_{11}$ cladding mode has a higher loss value than that of the $H^x{}_{11}$ core mode around $R \sim 1445\,\mu$m, since the bending radius is now significantly reduced. Its loss value also peaks near the degeneration point, $R \sim 835\,\mu$m, by being mixed with a higher loss cladding mode. Similarly, the loss value of the cladding mode is reduced near the degeneration point, due to being mixed with a lower loss core mode.

To understand the modal properties of this cladding mode at the lower bending radius range, the corresponding field plots are shown. The H^y field profile along the x axis for the $H^y{}_{11}$ core mode is shown in Fig. 10, when $R = 840\,\mu$m, just right of the degeneration point. The existence of a second peak between the first and the second airhole rings is clearly visible. In this case, the secondary peak is of a higher magnitude, as the local equivalent refractive index is much higher due to a smaller bending radius being

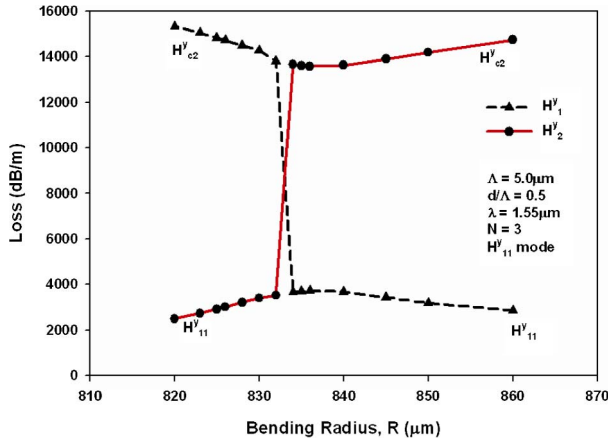

Fig. 9. (Color online) Variation of the total losses with the bending radius R.

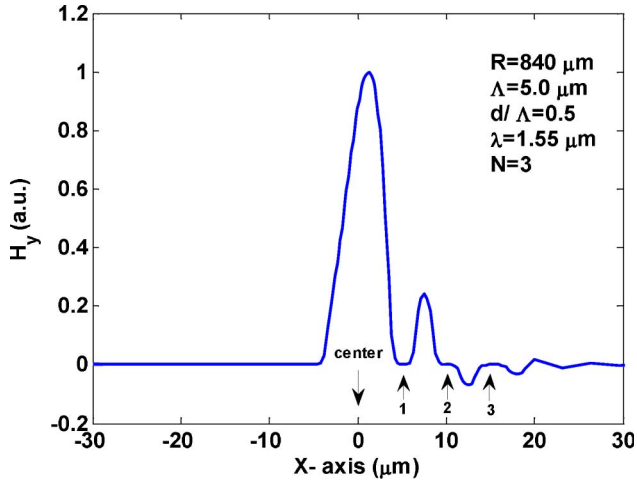

Fig. 10. (Color online) H_y field profile along the X axis for the $H^y{}_{11}$ core mode when $R = 840\,\mu$m above the degeneration point.

considered here. The H_y field profile of the $H^y{}_{11}$ core mode when $R = 830\,\mu$m, just left of the degeneration point, is shown in Fig. 11. In this case, the secondary peaks are also clearly visible. However, the change in its sign indicates that this mode is now a higher order mode, as its eigenvalue position has been shifted by the cladding mode.

The two-dimensional (2D) H_y contour of the $H^y{}_{c2}$ cladding mode just below the degeneration point, when $R = 833\,\mu$m, is shown in Fig. 12. The locations of the airholes are also shown by circles. It can be clearly observed that the modal field is confined in the silica bridge region between the first and the second airhole rings. It can also be noticed that the field spreads to link the three silica bridging areas. However, one feature is very clear: that this is a higher order cladding mode with two positive and negative peaks shown by different colored contours. It should also be noted that the local equivalent index value between the first and the second airhole rings would be lower than that between second and third airhole rings. Thus, with this cladding mode also being a

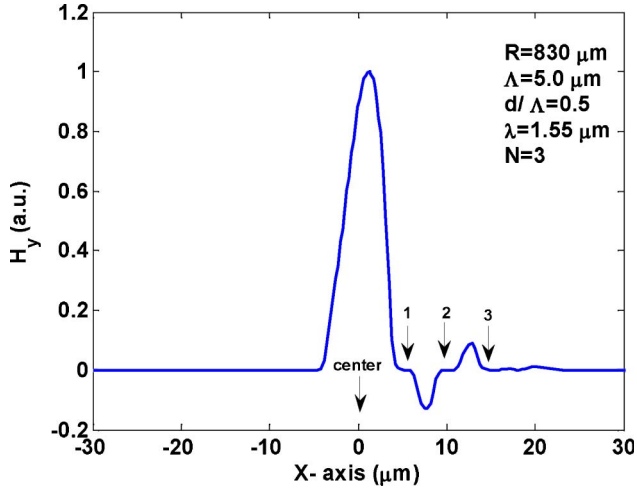

Fig. 11. (Color online) H_y field profile along the X axis for the $H^y{}_{11}$ core when $R = 830\,\mu$m below the degeneration point.

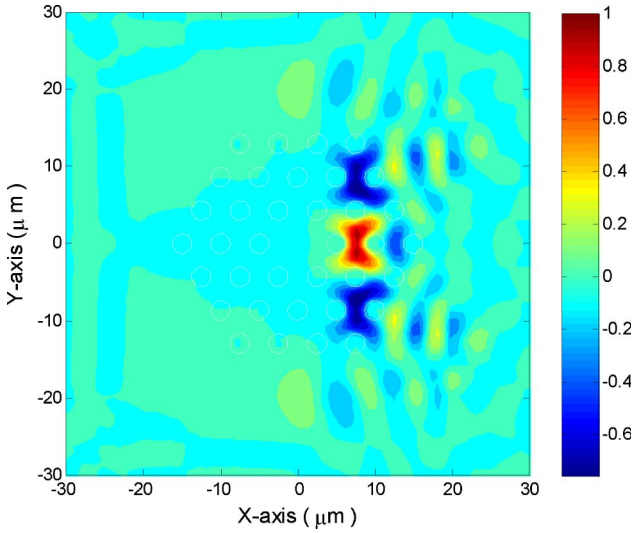

Fig. 12. (Color online) H_y contour of the higher order cladding mode when $R = 833\,\mu$m.

higher order mode, its effective index is significantly lower (compared to H^x_{c1}, shown in Fig. 5) for a larger bending radius. Hence, its effective index value only crosses that of the fundamental core mode at a much lower bending radius, when this value is increased significantly.

3. Conclusions

The above figures clearly show the origin of localized cladding modes in the silica bridging regions between the airholes. These areas are smaller than the PCF core (where an airhole is missing) and for a straight PCF, those modes with the lower effective indices do not interact with the PCF core mode. However, for a bent PCF, as the local equivalent index is increased, the dispersion slopes of these modes are higher, and for smaller bending radii they can be phase matched to the core mode to form coupled supermodes. It is also shown that these cladding modes can also cover several bridging regions simultaneously and also support the higher order modes. This mode degeneration causes a mixing of these modes, the formation of the supermodes and the transformation from one mode to another. These cause rapid changes in their modal properties and the effective index, the spot size, and the bending loss values. A higher pitch value or larger d/Λ ratio increases the silica bridging regions, and such mode degeneration can appear at a higher bending radius, which may often be encountered in practical applications. In these cases, the mode degeneration appears more frequently and shows as noisy loss values in experimental measurements [32,39].

The origin of these fundamental and higher order cladding modes, the coupling between them, and ultimately the coupling of these cladding supermodes with the fundamental core mode can affect the design of various PCF-based applications. The study of this mode degeneration gives insight to the practical application of PCFs and the optimum handing conditions during many "real world" applications. This understanding can also be useful in the study of PCF-based devices, thereby exploiting bending loss, for example by using effectively single mode waveguides with differential modal losses and single polarization waveguides with highly differential polarization dependent bending losses, or additionally, in the design of optical attenuators, for example.

References

1. P. St. J. Russell, "Photonic-crystal fibers," J. Lightwave Technol. **24**, 4729–4749 (2006).
2. B. E. Little, S. T. Chu, H. A. Haus, J. Foresi, and J. P. Laine, "Microring resonator channel dropping filters," J. Lightwave Technol. **15**, 998–1005 (1997).
3. M. Zirngibl, C. H. Joyner, L. W. Stulz, Th. Gaiffe, and C. Dragone, "Polarization independent 8 × 8 waveguide grating multiplexers on InP," Electron. Lett. **29**, 201–202 (1993).
4. R. R. Hayes and D. Yap, "GaAs spiral optical waveguides for delay-line applications," J. Lightwave Technol. **11**, 523–528 (1993).
5. X. Jiang, W. Qi, H. Zhang, Y. Tang, Y. Hao, J. Yang, and M. Wang, "Loss crosstalk 1 × 2 thermooptic digital optical switch with integrated *S*-bend attenuator," IEEE Photon. Technol. Lett. **18**, 610–612 (2006).
6. K. Saitoh, N. J. Florous, M. Koshiba, and M. Skorobogatiy, "Design of narrow band-pass filters based on the resonant-tunneling phenomenon in multi-core photonic crystal fibers," Opt. Express **13**, 10327–10335 (2005).
7. K. Iizawa, S. K. Varshney, Y. Tsuchida, K. Saitoh, and M. Koshiba, "Bend-insensitive lasing characteristics of single-mode, large-mode-area Ytterbium-doped photonic crystal fiber," Opt. Express **16**, 579–591 (2008).
8. M. van Eijkelenborg, J. Canning, T. Ryan, and K. Lyytikainen, "Bending-induced coloring in a photonic crystal fiber," Opt. Express **7**, 88–94 (2000).
9. J. Olszewski, M. Szpulak, and W. Urbańczyk, "Effect of coupling between fundamental and cladding modes on bending losses in photonic crystal fibers," Opt. Express **13**, 6015–6022 (2005).
10. J. C. Knight, T. A. Birks, P. St. J. Russell, and J. P. de Sandro, "Properties of photonic crystal fiber and the effective index model," J. Opt. Soc. Am. A **15**, 748–752 (1998).
11. J. Arriaga, J. C. Knight, and P. St. J. Russell, "Modeling the propagation of light in photonic crystal fibers," Physica D (Amsterdam) **189**, 100–106 (2004).
12. T. M. Monro, D. J. Richardson, N. G. R. Broderick, and P. J. Bennett, "Holey optical fibers: an efficient modal model," J. Lightwave Technol. **17**, 1093–1102 (1999).
13. T. P. White, R. C. McPhedran, C. M. de Sterke, L. C. Botten, and M. J. Steel, "Confinement losses in microstructured optical fibers," Opt. Lett. **26**, 1660–1662 (2001).
14. W. Zhi, R. Guobin, L. Shuqin, and J. Shuisheng, "Supercell lattice method for photonic crystal fibers," Opt. Express **11**, 980–991 (2003).
15. J. Riishede, N. A. Mortensen, and J. Lægsgaard, "A "poor man's approach" to modelling micro-structured optical fibres," J. Opt. A Pure Appl. Opt. **5**, 534–538 (2003).
16. B. M. A. Rahman, A. K. M. S. Kabir, M. Rajarajan, and K. T. V. Grattan, "Finite element modal solutions of planar photonic crystal fibers with rectangular air-holes," Opt. Quantum Electron. **37**, 171–183 (2005).
17. F. Fogli, L. Saccomandi, P. Bassi, G. Bellanca, and S. Trillo, "Full vectorial BPM modeling of index-guiding photonic crystal fibers and couplers," Opt. Express **10**, 54–59 (2002).

18. B. M. A. Rahman and J. B. Davies, "Finite-element solution of integrated optical waveguides," J. Lightwave Technol. **2**, 682–688 (1984).
19. N. Kejalakshmy, B. M. A. Rahman, A. K. M. S. Kabir, M. Rajarajan, and K. T. V. Grattan, "Single mode operation of photonic crystal fiber using a full vectorial finite element method," Proc. SPIE **6588**, 65880T (2007).
20. M. Heiblum and J. H. Harris, "Analysis of curved optical waveguides by conformal transformation," IEEE J. Quantum Electron. **11**, 75–83 (1975).
21. P. Bienstman, E. Six, M. Roelens, M. Vanwolleghem, and R. Baets, "Calculation of bending losses in dielectric waveguides using eigenmode expansion and perfectly matched layers," IEEE Photon. Technol. Lett. **14**, 164–166 (2002).
22. J. Gu, P. Besse, and H. Melchior, "Novel method for analysis of curved optical rib-waveguides," Electron. Lett. **25**, 278–280 (1989).
23. S. Kim and A. Gopinath, "Vector analysis of optical dielectric waveguide bends using finite-difference method," J. Lightwave Technol. **14**, 2085–2092 (1996).
24. F. Wassmann, "Modal field analysis of circularly bent single-mode fibers," J. Lightwave Technol. **17**, 957–968 (1999).
25. K. Thyagarajan, M. R. Shenoy, and A. K. Ghatak, "Accurate numerical method for the calculation of bending loss in optical waveguides using a matrix approach," Opt. Lett. **12**, 296–298 (1987).
26. W. Berglund and A. Gopinath, "WKB analysis of bend losses in optical waveguides," J. Lightwave Technol. **18**, 1161–1166 (2000).
27. T. Yamamoto and M. Koshiba, "Numerical analysis of curvature loss in optical waveguides by the finite-element method," J. Lightwave Technol. **11**, 1579–1583 (1993).
28. K. Saitoh, Y. Tsuchida, M. Koshiba, and N. A. Mortensen, "Endlessly single-mode holey fibers: the influence of core design," Opt. Express **13**, 10833–10839 (2005).
29. R. Jedidi and R. Pierre, "High-order finite-element method for the computation of bending loss in optical waveguides," J. Lightwave Technol. **25**, 2618–2630 (2007).
30. R. Baets and P. E. Lagasse, "Loss calculation and design of arbitrarily curved integrated-optic waveguides," J. Opt. Soc. Am. **73**, 177–182 (1983).
31. M. Rajarajan, S. S. A. Obayya, B. M. A. Rahman, K. T. V. Grattan, and H. A. El-Mikathi, "Characterization of low-loss waveguide bends with offset optimisation for compact photonic integrated circuits," IEE Proc. Optoelectron. **147**, 382–388 (2000).
32. N. H. Vu, I. Hwang, and Y. Lee, "Bending loss analyses of photonic crystal fibers based on the finite-difference time-domain method," Opt. Lett. **33**, 119–121 (2008).
33. H. F. Taylor, "Bending effects in optical fibers," J. Lightwave Technol. **2**, 617–628 (1984).
34. A. Argyros, T. Birks, S. Leon-Saval, C. M. B. Cordeiro, and P. St. J. Russell, "Guidance properties of low-contrast photonic bandgap fibers," Opt. Express **13**, 2503–2511 (2005).
35. F. L. Teixeira and W. C. Chew, "General closed-form PML constitutive tensors to match arbitrary bianisotropic and dispersive linear media," IEEE Microwave Guid. Wave Lett. **8**, 223–225 (1998).
36. M. Koshiba and K. Saitoh, "Full-vectorial imaginary-distance beam propagation method based on a finite element scheme: application to photonic crystal fibers," IEEE J. Quantum Electron. **38** 927–933 (2002).
37. A. Taflove and S. C. Hagness, *Computational Electrodynamics* (Artech House, 2000).
38. T. Martynkien, J. Olszewski, M. Szpulak, G. Golojuch, W. Urbanczyk, T. Nasilowski, F. Berghmans, and H. Thienpont, "Experimental investigations of bending loss oscillations in large mode area photonic crystal fibers," Opt. Express **15**, 13547–13556 (2007).
39. M. Koshiba and K. Saitoh, "Structural dependence of effective area and mode field diameter for holey fibers," Opt. Express **11**, 1746–1756 (2003).